

Article

Skull Melting Growth and Characterization of $(\text{ZrO}_2)_{0.89}(\text{Sc}_2\text{O}_3)_{0.1}(\text{CeO}_2)_{0.01}$ Crystals

Dmitrii Agarkov ^{1,2}, Mikhail Borik ³, Galina Eliseeva ¹, Alexey Kulebyakin ³, Elena Lomonova ³, Filipp Milovich ^{3,4,*}, Valentina Myzina ³, Yuriy Parkhomenko ^{4,5}, Elena Skryleva ⁴ and Nataliya Tabachkova ^{3,4}

¹ Institute of Solid State Physics, Russian Academy of Sciences, Academician Osip'yan str. 2, Chernogolovka, 142432 Moscow, Russia; agarkov@issp.ac.ru (D.A.); eliseevagm@issp.ac.ru (G.E.)

² Moscow Institute of Physics and Technology, Institutskiy per. 9, Dolgoprudny, 141701 Moscow, Russia

³ Prokhorov General Physics Institute, Russian Academy of Sciences, VavilovStr. 38, 119991 Moscow, Russia; borik@lst.gpi.ru (M.B.); kulebyakin@lst.gpi.ru (A.K.); lomonova@lst.gpi.ru (E.L.); vamyzina@lst.gpi.ru (V.M.); ntabachkova@gmail.com (N.T.)

⁴ National University of Science and Technology (MISIS), Leninskiy prospekt 4, 119049 Moscow, Russia; parkh@rambler.ru (Y.P.); skryleva.ea@misis.ru (E.S.)

⁵ State Scientific-Research and Design Institute of Rare-Metal Industry "Giredmet" JSC, B. Tolmachevsky per. 5-1, 119017 Moscow, Russia

* Correspondence: philippmilovich@gmail.com

Received: 26 December 2019; Accepted: 17 January 2020; Published: 19 January 2020



Abstract: $(\text{ZrO}_2)_{0.89}(\text{Sc}_2\text{O}_3)_{0.1}(\text{CeO}_2)_{0.01}$ crystals have been grown by directional melt crystallization in a cold crucible. The chemical and phase compositions of the crystals have been characterized using energy dispersion X-ray spectroscopy (EDX), Raman scattering spectroscopy and transmission electron microscopy (TEM). The X-ray photoelectron emission method has been used for determining the valence state of the Ce ions. We show that directional melt crystallization produces an inhomogeneous ceria distribution along the crystal length. The as-grown crystals are mixtures of cubic and rhombohedral zirconia modifications. The rhombohedral phase has an inhomogeneous distribution along crystal length. Melt crystallization does not produce single-phase cubic $(\text{ZrO}_2)_{0.89}(\text{Sc}_2\text{O}_3)_{0.1}(\text{CeO}_2)_{0.01}$ crystals. The formation of the phase structure in the crystals for different synthesis methods has been discussed.

Keywords: directional solidification; growth from melt; $\text{ZrO}_2\text{-Sc}_2\text{O}_3\text{-CeO}_2$; dielectric materials; solid electrolytes

1. Introduction

Scandia-stabilized zirconia solid solutions have high oxygen ionic conductivity and show good promise for the production of solid-state electrolytes for electrochemical devices, e.g., solid oxide fuel cells (SOFCs). The highest conductivity for the $\text{ZrO}_2\text{-Sc}_2\text{O}_3$ system was observed in compositions containing 8–12 mol.% of Sc_2O_3 which had a stable cubic structure at 700–800 °C. With a decrease in temperature, the high-conductivity cubic phase transforms to the rhombohedral β -phase, and the ionic conductivity of these materials decreases dramatically. Earlier data [1–3] showed that the formation of the rhombohedral phase in the $\text{ZrO}_2\text{-Sc}_2\text{O}_3$ system solid solutions occurs by ordering of the oxygen vacancies. However, there are indications of cubic phase stabilization in ZrO_2 ceramics containing 12 mol.% of Sc_2O_3 [4,5]. The formation of the rhombohedral phase in these specimens was attributed to a homogeneous distribution of the Sc^{3+} cations in the ZrO_2 matrix, which is achieved due to a low heating rate (~ 2 °C/min) during solid state synthesis and the presence of a small quantity of impurities [5]. This may destroy the long-range order of the oxygen vacancies and favor the

stabilization of the cubic c-phase. The formation of the rhombohedral β -phase in the low-temperature range can also be avoided by co-doping with small quantities of some oxides (Gd_2O_3 [6], CeO_2 [6], Y_2O_3 [4], Yb_2O_3 [7]). For example, introduction of CeO_2 into the ZrO_2 – Sc_2O_3 system stabilizes the cubic phase since the larger Ce^{4+} ions (ionic radius of $\text{Ce}(\text{VIII})^{4+} = 0.97 \text{ \AA}$) compared with that of the Zr^{4+} ions (0.84 \AA) favor the localization of the vacancies in the vicinity of the Zr^{4+} cations, thus suppressing the formation of the low-symmetry rhombohedral phase [8]. The most promising composition in the ZrO_2 – Sc_2O_3 – CeO_2 system is the one containing 10 mol.% of Sc_2O_3 and 1 mol.% of CeO_2 (10Sc1CeSZ), which has the highest conductivity and highly stable properties under long-term exposure to SOFC working temperatures [9,10].

In our previous work [11], we studied the structural and transport properties of $(\text{ZrO}_2)_{1-x-y}(\text{Sc}_2\text{O}_3)_x(\text{CeO}_2)_y$ solid solution crystals ($x = 0.08$ – 0.10 ; $y = 0.005$ – 0.015) grown by directional melt crystallization. We found that this synthesis method does not provide single-phase cubic crystals of the studied composition range at room temperature, which is contradictory to the phase analysis data for specimens synthesized using various ceramic technologies. We studied, in detail, the phase composition of the $(\text{ZrO}_2)_{0.89}(\text{Sc}_2\text{O}_3)_{0.1}(\text{CeO}_2)_{0.01}$ (10Sc1CeSZ) specimen in this work and investigated the factors affecting the formation of the crystal structure in this synthesis method. Also, we report data on the behavior of Ce ions during the melt synthesis.

2. Materials and Methods

$(\text{ZrO}_2)_{0.89}(\text{Sc}_2\text{O}_3)_{0.1}(\text{CeO}_2)_{0.01}$ solid solution crystals were grown by directional melt crystallization in a cold crucible [12]. The crystals were grown by directed crystallization of the melt in a water-cooled copper container using direct high-frequency (5.28 MHz) material heating. The power of the high-frequency generator was 60 kW. The charge was prepared from min. 99.99% purity ZrO_2 , Sc_2O_3 , and CeO_2 powders. The starting oxides, with a total weight of 6 kg, were pre-mixed mechanically and placed in a container. Metallic zirconium in the charge was used for starting heating. The melt crystallization rate was 10 mm/h. High-frequency heating was ceased after the end of the crystallization process. Further spontaneous cooling of the crystallized ingot occurred. The temperature of the ingot surface was recorded with a Gulton 900–1999 radiation pyrometer in a 2000–1000 °C range and a Pt/Pt-Rh thermocouple in the 1000–500 °C range; the ingot cooling rates in these temperature ranges were $\sim 200 \text{ }^\circ\text{C}/\text{min}$ and $\sim 30 \text{ }^\circ\text{C}/\text{min}$, respectively.

The chemical composition of the as-grown crystals was examined with a JEOL 5910 LV scanning electron microscope (JEOL, Tokyo, Kanto, Japan) with an energy-dispersive AZtecENERGY analytical system equipped (Oxford Instruments, X-Max-80, Abingdon, UK). The references were molten ZrO_2 , Sc_2O_3 and CeO_2 .

Phase analysis was performed by X-ray diffraction on a Bruker D8 diffractometer (Bruker, Billerica, MA, USA) using $\text{CuK}\alpha$ radiation. The specimens were cut in the form of plates perpendicular to the $\langle 100 \rangle$ direction. For phase analysis, planes with different indexes and different phases were set to the reflecting position. Raman spectra of the specimens were recorded on a Renishaw inVia Raman microscopic spectrometer (Renishaw, Wotton-under-Edge, Gloucestershire, UK) ($\lambda_{\text{exc.}} = 532 \text{ nm}$) and with a home-made Raman setup that was described in previous works [13,14]. The crystal structure was studied using transmission electron microscopy at a 200 kV accelerating voltage with a JEM-2100 microscope (JEOL, Tokyo, Kanto, Japan). The specimens were prepared by ion etching on a PIPS II (GATAN, Milton Abingdon, UK) setup.

XPS analyses were performed on PHI 5000 VersaProbe II equipment (Physical Electronics, Chanhassen, MN, USA) using monochromatic $\text{AlK}\alpha$ radiation with a focused beam diameter of 200 μm . High-resolution (HR) spectra were acquired at an analyzer pass energy of 29.35 eV in increments of 0.25 eV. The binding energy (BE) of adsorbed hydrocarbons peak C1s (285.0 eV) was used as a reference value for adjusting the BE scale. Samples for analysis were obtained by cleaving crystals immediately before loading into the spectrometer. The electrostatic charge caused by photoelectron emission of the dielectric samples was compensated by a charge neutralization system.

3. Results and Discussion

Literary data described several types of $\text{ZrO}_2\text{-Sc}_2\text{O}_3$ system phase diagrams distinguished by the presence of a number of metastable phases in the solidus region [15–17]. It should be noted that the greatest differences between these phase diagrams are observed at temperatures below 1400 °C. However, their common feature, just like for the $\text{ZrO}_2\text{-Y}_2\text{O}_3$ phase diagram, is a high-temperature range of cubic solid solutions (at a stabilizing oxide concentration of 10 mol.%). Therefore, melt-grown 10Sc1CeSZ crystals have a cubic structure, which is retained during cooling until the bottom temperature limit of cubic phase existence. The high-temperature cubic phase is stable up to a temperature of ~600 °C for a given composition [17]. Further cooling to room temperature may entail a phase transition to one of the room-temperature stable solid solution modifications (monoclinic, tetragonal or rhombohedral).

The ingot grown by directional melt crystallization contained separate crystals, which had a pillar shape typical of this synthesis method. The lateral crystal dimensions increased with a decrease in the directional crystallization rate from 10 to 3 mm/h, the maximum crystal size being 50 mm in length and a cross-section of 25 mm. Figure 1a shows the typical as-grown crystal appearance. The as-grown crystals had a dark-red color.



Figure 1. Appearance (a) and cross-section (b) of as-grown crystal.

Figure 1b shows a plate cut along the crystal growth axis, which clearly shows a non-uniform color distribution in the crystal bulk. The color intensity is lower at the crystal periphery, resulting in colorless regions on the crystal surface, testifying to a decrease in the concentration of the Ce^{3+} cations, which have absorption bands in the visible spectral region and change the color of the crystals to orange-red [18]. Ingot air cooling causes Ce^{3+} ions to oxidize to Ce^{4+} , this process occurs at the crystal periphery. Since an ingot consisting of separate crystals cools down quite rapidly and the oxygen diffusion coefficient decreases dramatically with decreasing temperature, oxygen does not

have sufficient time to diffuse to the entire crystal bulk. The darker color of the crystal top part suggests a higher Ce^{3+} ion concentration.

Figure 2 shows data on component distribution along the 10Sc1CeSZ crystal length suggesting cerium oxide displacement toward the crystal top part during directional crystallization. A similar behavior was observed in cerium-doped cubic $\text{ZrO}_2\text{-Y}_2\text{O}_3$ crystals where the effective cerium distribution coefficient was ~ 0.5 [16,18]. An increase in the impurity concentration at the end of the growth may violate normal crystallization conditions due to constitutional undercooling at the crystallization front causing growth defect formation in the form of growth bands with an elevated concentration of the displaced impurity, cellular structure, inclusions, etc. These defects are most typical of crystals growing in the central part of solidified melt ingots since the axial temperature gradients in the central part of the melt are lower than those at the periphery. This results from specific features of direct high-frequency heating of dielectrics in a cold crucible [16,18].

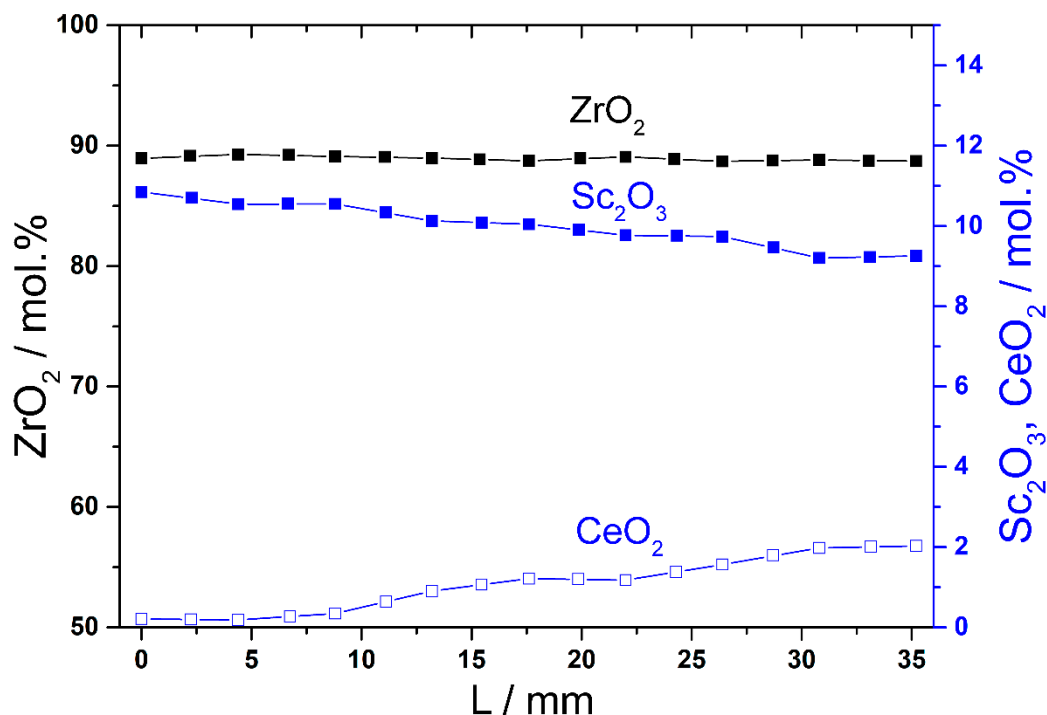


Figure 2. Zirconia scandia and ceria distribution along the length of the crystal 10Sc1CeSZ.

It can be seen clearly that, at an early growth stage, the ceria concentration in the solid solution is lower than 1 mol.%; in the central crystal part, it is almost equal to 1 mol.%; by the end of the growth, it increases to 1.5–2 mol.%. In the meantime, the scandia concentration decreases along the crystal.

Qualitative assessment of the Ce^{3+} ion distribution in the crystal length was also carried out using Raman spectroscopy based on the intensity of the peak near 2200 cm^{-1} corresponding to the ${}^2\text{F}_{7/2}\text{-}{}^2\text{F}_{5/2}$ electron transition in the Ce^{3+} ions [19]. Figure 3 shows Raman spectra for different 10Sc1CeSZ crystal regions. It can be seen that the intensity of the peak characterizing the concentration of the Ce^{3+} ions increases in the top part of the crystal (Figure 3b). This is in agreement with the experimentally observed change in the crystal color along the length of the crystal.

Thus, directional melt crystallization is accompanied not only by an increase in the overall ceria concentration but also by an increase in the Ce^{3+} ion concentration in the crystal. In the meantime, the scandia concentration decreases along the crystal.

We used high-resolution X-ray photoelectron spectroscopy for quantitative evaluation of the Ce ion concentration for different valence states. Figure 4 shows the Ce3d high-resolution X-ray photoelectron spectrum for the as-grown 10Sc1CeSZ crystal which was obtained in the same analysis

area, with a diameter of 200 μm and at the following time intervals: 0.5, 1 and 48 h after loading and preliminary pumping in the chamber at 5×10^{-6} Pa. The approximation of the Ce3d doublet spectra (spin-orbit splitting into $3d_{5/2}$ and $3d_{3/2}$ peaks), which have a complex shape due to the presence of satellites structure due to multi-electron interactions, revealed the presence of VU, V''-U'' and V'' doublets -U''' from Ce^{4+} ions and also Vo-Uo doublets, V'-U' from Ce^{3+} ions.

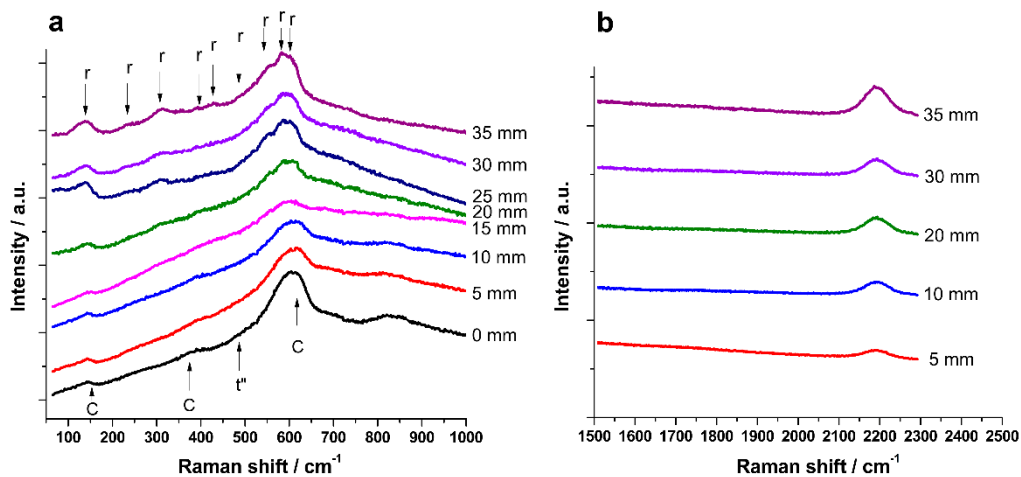


Figure 3. Raman spectra along as-grown 10Sc1CeSZ crystal.

The fraction of Ce^{3+} ions was determined according to the widely used quantitative method [20,21], as the sum of the relative intensities of the Vo-Uo, V'-U' peaks in the full Ce3d spectrum. However, the effect of cerium reduction was clearly manifested in this work during research under high-vacuum conditions of 5×10^{-8} Pa and irradiation by focused X-ray radiation with a diameter of 200 μm and a power of 50 W. A noticeable decrease in the intensity of the peaks corresponding to Ce^{4+} was observed after 1 and 48 h of exposure of the sample in vacuum, as can be seen from Figure 4a–c. Estimation of the fraction of Ce^{3+} ions showed values of 40%, 50%, and 60%, respectively, depending on the exposure time of the sample in the chamber (0.5, 1, and 48 h). The effect of cerium reduction is well known in studies using this method. As was shown in [22], the exposure of CeO_2 powders in vacuum, the effect of X-ray radiation, and the surface charge effect of the sample affect the charge state of Ce ions. However, the reduction effect of cerium ions manifests itself more noticeably in our case when studying the surface of the cleaved crystal.

X-ray diffraction study of the phase composition of the crystals showed that the crystals consist of two phases, i.e., the cubic and the rhombohedral ones. Raman spectroscopy study of the crystal structure confirms the presence of these two phases (Figure 3a). The general pattern of the Raman spectra is similar to that observed earlier [23,24] for $\text{ZrO}_2\text{-Sc}_2\text{O}_3$ system specimens and contains cubic and rhombohedral phase bands. The intensity of the bands corresponding to the rhombohedral phase increases at the end of the crystal, with the bands becoming more pronounced. Thus, the rhombohedral phase concentration increases along the 10Sc1CeSZ crystal length during directional crystallization.

Figure 5 shows TEM images of two regions in the bottom and top parts of the crystal. The bottom part of the crystal contains inclusions of large rhombohedral phase twins in the cubic matrix. The top part of the crystal consists mainly of rhombohedral phase twins. No twin-free rhombohedral phase regions are observed.

Thus, the Raman spectroscopy and TEM results suggest an inhomogeneous rhombohedral phase distribution along the crystal length: the rhombohedral phase content in the top part of the crystal is higher than that in its bottom part. The observed inhomogeneous distribution of the rhombohedral phase along the crystal length may be due to changes in the chemical composition along the crystal length, namely, changes in the total content of ceria, changes in the ratio of $\text{Ce}^{3+}/\text{Ce}^{4+}$, and changes in the scandia content.

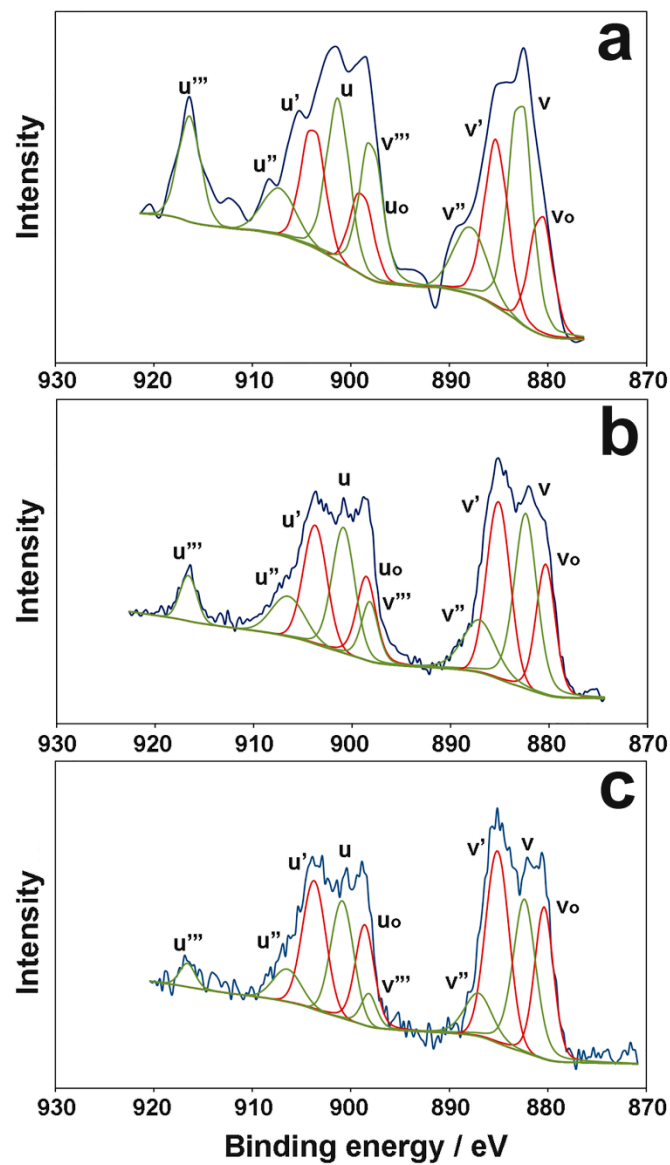


Figure 4. (Color online) Ce3d photoelectron spectra for as-grown 10Sc1CeSZ crystal after 30 min (a), 1 h (b) and 48 h (c) in the test chamber. The experimental spectra (blue lines) were fitted using V-U, V''-U'' and V'''-U''' doublets from Ce⁴⁺ (green lines) and Vo-Uo, V'-U' doublets from Ce³⁺ (red lines).

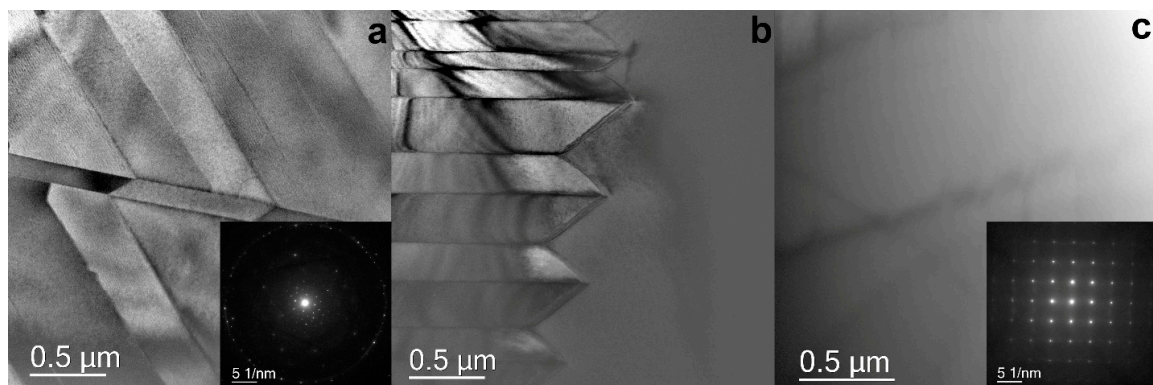


Figure 5. TEM images of top (a) and bottom (b,c) parts of 10Sc1CeSZ crystal. Insets: electron diffraction patterns of the respective crystal regions.

Unlike the single-phase cubic 10Sc1CeSZ specimens synthesized using the ceramic technology, 10Sc1CeSZ crystallization from melt did not provide for cubic phase stabilization in the entire crystal bulk.

We can specify several substantial differences which may affect cubic phase stabilization in the melt-grown and the ceramic 10Sc1CeSZ specimens. First, cubic phase stabilization in the ceramic specimens occurs during sintering in a specific temperature range. If Daiichi Kigenso Kagaku Kogyo (DKKK) and Praxair powders were used as the source material, single-phase cubic specimens were only obtained at sintering temperatures of >1300 °C [25]. For coprecipitated powders, the respective temperature was 1500 °C [26]. The thermal conditions of the synthesis for the melt-crystallization-grown specimens differed considerably from those for the synthesis of ceramics. For directional crystallization from melt, the crystals start to grow at the crystallization front at the solidus temperature (~ 2800 °C). Then, as the crystals grow, the crystalline ingot first cools down gradually to 1200–1400 °C, and further cooling to room temperature occurs spontaneous.

Secondly, ceramic technologies typically use source materials containing considerable (to 2 mol.%) quantities of impurities such as Si, Na, Ti and Al [24,26]. The materials used for crystal growth are of much higher purity and, furthermore, directional crystallization causes additional crystal purification due to impurity displacement or evaporation.

Thirdly, the presence of grain boundaries in ceramic specimens can stabilize the high-temperature phases due to impurity segregation and inhomogeneous distribution of the stabilizing oxides in the grain volume.

Furthermore, it is believed that cerium ions exist in the solid solution of 10Sc1CeSZ ceramic specimens in the form of Ce^{4+} ions [27]. One can assume that the combination of these factors determines the final phase composition of the crystals. It should be, however, noted that in spite of the abovementioned differences between the specimens synthesized using the ceramic technology and those grown by crystallization from melt, single phase cubic crystals were obtained in the ZrO_2 – Sc_2O_3 – Y_2O_3 systems [28].

Thus, the predominant factor in the growth of 10Sc1CeSZ crystals determining their phase composition is the presence of cerium ions having variable valence (Ce^{3+} or Ce^{4+}).

4. Concluding Remarks

$(ZrO_2)_{0.89}(Sc_2O_3)_{0.1}(CeO_2)_{0.01}$ crystals up to 50 mm in length and with a cross-section of up to 25 mm were grown using directional melt crystallization. Cerium ions exist in the as-grown crystals in the form of Ce^{3+} and Ce^{4+} ions. Study of the crystals showed that directional melt crystallization increases not only the overall ceria concentration but also the Ce^{3+} ion content along the length of the crystals. X-ray diffraction, Raman spectroscopy and transmission electron microscopy studies of the phase composition of the crystals showed that the as-grown crystals are mixtures of cubic and rhombohedral zirconia modifications. The rhombohedral phase has an inhomogeneous distribution along the crystals: the rhombohedral phase content is higher in the top part of the crystal than in the bottom part. Rhombohedral phase contains twins, which have a large size. Thus, unlike single-phase cubic 10Sc1CeSZ specimens synthesized using the ceramic technology, 10Sc1CeSZ crystallization from the melt did not promote cubic phase stabilization in the entire crystal bulk.

Author Contributions: Conceptualization: N.T., E.L. Methodology: N.T., F.M., E.S., E.L., V.M. Software: F.M. Formal analysis: N.T., D.A., G.E., F.M., E.S., A.K. Writing—original draft preparation: N.T., E.L. Writing—review and editing: N.T., E.L., M.B. Visualization: F.M. Project administration: E.L. Funding acquisition: Y.P. All authors have read and agreed to the published version of the manuscript.

Funding: This work was carried out within Russian Science Foundation (RSF) grant No.16-13-00056.

Acknowledgments: The Authors thank the Research Center “Materials Science and Metallurgy” NUST “MISIS”.

Conflicts of Interest: The authors declare no conflict of interest.

References

1. Thomber, M.R.; Bevan, D.J.M.; Summerville, E. Mixed oxides of the type MO_2 (fluorite)- M_2O_3 . V. phase studies in the systems ZrO_2 - M_2O_3 ($\text{M} = \text{Sc}, \text{Yb}, \text{Er}, \text{Dy}$). *J. Solid State Chem.* **1970**, *1*, 545–553. [[CrossRef](#)]
2. Ishii, T.; Iwata, T.; Tajima, Y.; Yamaji, A. Structural phase transition and ion conductivity in 0.88ZrO_2 - $0.12\text{Sc}_2\text{O}_3$. *Solid State Ion.* **1992**, *57*, 153–157. [[CrossRef](#)]
3. Kondoh, J.; Tomii, Y.; Kawachi, K. Changes in Aging Behavior and Defect Structure of Yttria-Fully-Stabilized ZrO_2 with Sc_2O_3 Doping. *J. Am. Ceram. Soc.* **2003**, *86*, 2093–2102. [[CrossRef](#)]
4. Politova, T.I.; Irvine, J.T.S. Investigation of scandia-yttria-zirconia system as an electrolyte material for intermediate temperature fuel cells—Influence of yttria content in system $(\text{Y}_2\text{O}_3)_x(\text{Sc}_2\text{O}_3)_{(11-x)}(\text{ZrO}_2)_{89}$. *Solid State Ion.* **2004**, *168*, 153–165. [[CrossRef](#)]
5. Shukla, V.; Balani, K.; Subramaniam, A.; Omar, S. Phase stability and conductivity in the pseudo ternary system of $x\text{Yb}_2\text{O}_3$ - $(12-x)\text{Sc}_2\text{O}_3$ - 88ZrO_2 ($0 \leq x \leq 5$). *Solid State Ion.* **2019**, *332*, 93–101. [[CrossRef](#)]
6. Omar, S.; Bin Najib, W.; Chen, W.; Bonanos, N. Electrical conductivity of 10 mol% Sc_2O_3 -1 mol% M_2O_3 - ZrO_2 ceramics. *J. Am. Ceram. Soc.* **2012**, *95*, 1965–1972. [[CrossRef](#)]
7. Yuan, F.; Wang, J.; Miao, H.; Guo, C.; Wang, W.G. Investigation of the crystal structure and ionic conductivity in the ternary system $(\text{Yb}_2\text{O}_3)_x$ - $(\text{Sc}_2\text{O}_3)_{(0.11-x)}$ - $(\text{ZrO}_2)_{0.89}$ ($x = 0$ – 0.11). *J. Alloy. Compd.* **2013**, *549*, 200–205. [[CrossRef](#)]
8. Arachi, Y.; Asai, T.; Yamamoto, O.; Takeda, Y.; Imanishi, N.; Kawate, K.; Tamakoshi, C. Electrical conductivity of ZrO_2 , Sc_2O_3 doped with HfO_2 , CeO_2 and Ga_2O_3 . *J. Electrochem. Soc.* **2001**, *148*, A520–A523. [[CrossRef](#)]
9. Wang, Z.W.; Cheng, M.J.; Dong, Y.L.; Zhang, M. Anode-supported SOFC with 1Ce10ScZr modified cathode/electrolyte interface. *J. Power Sources* **2006**, *156*, 306–310. [[CrossRef](#)]
10. Tu, H.; Liu, X.; Yu, Q. Synthesis and Characterization of Scandia ceria stabilized zirconia powders prepared by polymeric precursor method for integration into anode-supported solid oxide fuel cells. *J. Power Sources* **2011**, *196*, 3109–3113. [[CrossRef](#)]
11. Agarkov, D.A.; Borik, M.A.; Bublik, V.T.; Bredikhin, S.I.; Chislovb, A.S.; Kulebyakin, A.V.; Kuritsyna, I.E.; Lomonova, E.E.; Milovich, F.O.; Myzina, V.A.; et al. Structure and transport properties of melt grown Sc_2O_3 and CeO_2 doped ZrO_2 crystals. *Solid State Ion.* **2018**, *85*, 24–29. [[CrossRef](#)]
12. Dhanaraj, G.; Byrappa, K.; Prasad, V.; Dudley, M. *Springer Handbook of Crystal Growth*; Dhanaraj, G.; Byrappa, K.; Prasad, V.; Dudley, M. Springer: New York, NY, USA, 2010; pp. 433–477.
13. Agarkov, D.A.; Burmistrov, I.N.; Tsybrov, F.M.; Tartakovskii, I.I.; Kharton, V.V.; Bredikhin, S.I. Kinetics of NiO reduction and morphological changes in composite anodes of solid oxide fuel cells: Estimate using Raman scattering technique. *Russ. J. Electrochem.* **2016**, *52*, 600–605. [[CrossRef](#)]
14. Agarkov, D.A.; Burmistrov, I.N.; Tsybrov, F.M.; Tartakovskii, I.I.; Kharton, V.V.; Bredikhin, S.I. In-situ Raman spectroscopy analysis of the interfaces between Ni-based SOFC anodes and stabilized zirconia electrolyte. *Solid State Ion.* **2017**, *302*, 133. [[CrossRef](#)]
15. Spiridonov, F.M.; Popova, L.N.; Popil'skii, R.Y.A. On the phase relations and the electrical conductivity in the system ZrO_2 - Sc_2O_3 . *J. Solid State Chem.* **1970**, *2*, 430–438. [[CrossRef](#)]
16. Ruh, R.; Garrett, H.J.; Domagala, R.F.; Patel, V.A. The System zirconia-scandia. *J. Am. Ceram. Soc.* **1977**, *60*, 399–403. [[CrossRef](#)]
17. Yashima, M.; Ishizawa, N.; Fujimori, H.; Kakihana, M.; Yoshimura, M. In-situ Observation of the Diffusionless Tetragonal to Cubic Phase Transition and Metastable-Stable Phase Diagram in the ZrO_2 - $\text{ScO}_1.5$ System. *Eur. J. Solid State Inorg. Chem.* **1995**, *32*, 761–770.
18. Kuz'minov, Y.S.; Lomonova, E.E.; Osiko, V.V. *Cubic Zirconia and Skull Melting*, 2nd ed.; Cambridge International Science Publishing Ltd.: Cambridge, UK, 2008; pp. 346–349.
19. Otake, T.; Yugami, H.; Naito, H.; Kawamura, K.; Kawada, T.; Mizusaki, J. Ce^{3+} concentration in ZrO_2 - CeO_2 - Y_2O_3 system studied by electronic Raman scattering. *Solid State Ion.* **2000**, *135*, 663–667. [[CrossRef](#)]
20. El Fallah, J.; Hilaire, L.; Roméo, M.; Le Normand, F. Effect of surface treatments, photon and electron impacts on the ceria 3d level. *J. Electron Spectrosc. Relat. Phenom.* **1995**, *73*, 89–103. [[CrossRef](#)]
21. Zhang, F.; Wang, P.; Koberstein, J.; Khalid, S.; Chan, S.W. Cerium oxidation state in ceria nanoparticles studied with X-ray photoelectron spectroscopy and absorption near edge spectroscopy. *Surf. Sci.* **2004**, *563*, 74–82. [[CrossRef](#)]

22. Paparazzo, E. Use and mis-use of x-ray photoemission spectroscopy Ce3d spectra of Ce₂O₃ and CeO₂. *J. Phys. Condens. Matter* **2018**, *30*, 100–128. [[CrossRef](#)]
23. Fujimori, H.; Yashima, M.; Kakihana, M.; Yoshimura, M. β -Cubic Phase Transition of Scandia-Doped Zirconia Solid Solution: Calorimetry X-ray Diffraction, and Raman Scattering. *J. Appl. Phys.* **2002**, *91*, 6493–6498. [[CrossRef](#)]
24. Fujimori, H.; Yashima, M.; Kakihana, M.; Yoshimura, M. Structural changes of scandia-doped zirconia solid solutions: Rietveld analysis and Raman scattering. *J. Am. Ceram. Soc.* **1998**, *81*, 2885–2893. [[CrossRef](#)]
25. Yarmolenko, S.; Sankar, J.; Bernier, N.; Klimov, M.; Kapat, J.; Orlovskaya, N. Phase stability and sintering behavior of 10mol% Sc₂O₃–1mol% CeO₂-ZrO₂ ceramics. *J. Fuel Cell Sci. Technol.* **2009**, *6*, 021007. [[CrossRef](#)]
26. Liu, Y.; Chen, X.; Yao, R.; Liao, S.; Chen, W.; Nie, D.; Zheng, F. Mechanical properties of 1 mol% CeO₂-10 mol% Sc₂O₃ co-doped and stabilized ZrO₂ synthesized through hydro/solve-thermal method. *Int. J. Appl. Ceram. Technol.* **2017**, *14*, 474–485. [[CrossRef](#)]
27. Omar, S.; Bonanos, N. Ionic conductivity ageing behaviour of 10 mol.% Sc₂O₃–1 mol.% CeO₂-ZrO₂ ceramics. *J. Mater. Sci.* **2010**, *45*, 6406–6410. [[CrossRef](#)]
28. Borik, M.A.; Bredikhin, S.I.; Bublik, V.T.; Kulebyakin, A.V.; Kuritsyna, I.E.; Lomonova, E.E.; Milovich, F.O.; Myzina, V.A.; Osiko, V.V.; Ryabochkina, P.A.; et al. Phase composition, structure and properties of (ZrO₂)_{1-x-y}(Sc₂O₃)_x(Y₂O₃)_y solid solution crystals (x = 0.08–0.11; y = 0.01–0.02) grown by directional crystallization of the melt. *J. Cryst. Growth* **2017**, *457*, 122–127. [[CrossRef](#)]



© 2020 by the authors. Licensee MDPI, Basel, Switzerland. This article is an open access article distributed under the terms and conditions of the Creative Commons Attribution (CC BY) license (<http://creativecommons.org/licenses/by/4.0/>).